

***Final Draft***  
**of the original manuscript:**

Ovri, H.; Steglich, D.; Dieringa, H.; Lilleodden, E.T.:  
**Grain-scale investigation of the anisotropy of Portevin-Le Chatelier effect  
in Mg AZ91 alloy.**

In: Materials Science and Engineering A. Vol. 740-741 (2019) 226 - 234.  
First published online by Elsevier: 24.10.2018

DOI: /10.1016/j.msea.2018.10.099  
<https://dx.doi.org/10.1016/j.msea.2018.10.099>

# Grain-scale investigation of the anisotropy of Portevin-Le Chatelier effect in Mg AZ91 alloy

Henry Ovri<sup>1\*</sup>, Dirk Steglich<sup>1</sup>, Hajo Dieringa<sup>2</sup>, Erica T. Lilleodden<sup>1,3</sup>

<sup>1</sup>Helmholtz Zentrum Geesthacht, Institute of Materials Research, Materials Mechanics, 21502 Geesthacht, Germany.

<sup>2</sup>Helmholtz Zentrum Geesthacht, Institute of Materials Research, Magnesium Innovation Centre, 21502 Geesthacht, Germany.

<sup>3</sup>Hamburg University of Technology, Institute of Advanced Ceramics, 21073 Hamburg, Germany.

## Abstract

An aspect of Portevin-Le Chatelier (PLC) type plastic instability that is yet to be understood is its orientation dependence. Such knowledge is crucial in view of its implications for texture weakening and, by extension, improvement in formability in Mg-based alloys. In this work, insight into the micromechanisms that govern PLC and its orientation dependence in single grains of Mg AZ91 is achieved using a combination of spherical nanoindentation, local orientation image analysis and crystal plasticity based finite element simulations, which was specifically used to identify the anisotropy in slip activity for the investigated orientations. Moreover, a statistical thermal activation model that is based on the distribution of load jumps between consecutive displacement bursts in the load vs. displacement response is presented. The paper demonstrates the ability of the model to predict the thermal activation parameters for the PLC effect. On the basis of the results, we propose a mechanistically sound model for the PLC effect that explains the underlying micromechanisms, the role of Al and Zn atoms, and the origin of the orientation dependence of the phenomenon. We also highlight the influence of the PLC effect on formability in Mg-based alloys.

**Keywords:** Magnesium alloy, nanoindentation, crystallographic misorientations, plastic instability, thermally activated processes, crystal plasticity

## 1 Introduction

Plasticity, particularly at the sub-micron scale, is hardly homogeneous. It is usually characterized by complex intermittent phenomena arising from both short- and long-range interactions between mobile dislocations and different types of obstacles that lie along the glide path of the dislocations [1][2]. Most of these intermittent phenomena are seldom observed at the macroscale since the length scales involved are orders of magnitude smaller than typical “rulers” applicable at the macroscale. One type of plastic instability, namely the Portevin–Le Chaterlier (PLC) effect, can however be observed across length scales that span the macro-, meso- and sub-micron scales [3][4]. This is of advantage since it directly provides the possibility of unravelling the underlying microscopic mechanisms that govern this phenomenon.

It is generally accepted that the PLC-type plastic instability in solution strengthened alloys systems is governed by the thermally activated release of solute clustered mobile dislocations from forest dislocations which are equally solute clustered [5]. The concentration of solutes that diffuse to and decorate both the temporarily trapped mobile dislocations and the forest dislocations are a function of the applied strain rate, deformation temperature and the average dislocation density [6][7]. Low strain rates and/or moderate-to-high temperatures increase the concentration of the solutes and consequently the magnitude of the pinning forces on the arrested dislocations and the forest junctions. Under these conditions, a material exhibits negative rate sensitivity (nSRS) since the local force required to release the solute clustered mobile dislocations from the clustered forest junctions is much higher than the force required to release the dislocations in the absence of solute clustering (strain aging).

PLC-type plastic instability has drawn a lot of interest because of deleterious effects associated with its occurrence. This is particularly true for Al-Mg based alloys where it is known to severely decrease formability and to degrade the surface quality of the alloy during

forming processes [4]. Recent work however seems to suggest that the phenomenon can be of advantage in some Mg alloys systems. Specifically, the texture weakening observed in Mg alloys with rare earth (RE) additions such as Ce, Gd, and Y have been associated with the PLC effect [8][9]. Wang and co-workers also observed similar effect in Mg with Ca addition [10]. These authors propose that the significant difference in atomic radii lead to a strong solute pinning effect which gives rise to nSRS. They argue that nSRS in turn promotes texture weakening and ultimately increases formability in these alloy systems. While this is plausible, we note that a physically sound model that clearly elucidates the underlying mechanisms connecting nSRS to texture weakening and is supported by experiments or simulations is yet elusive.

It is worth noting that in general, the formability of Mg is severely limited by the intrinsic plastic anisotropy of its HCP crystal. This anisotropy promotes the formation of basal texture in wrought Mg alloys since the basal slip system is the system with the lowest critical resolved shear stress (CRSS) in the HCP crystal [10]. Fundamental understanding of the role of PLC-type plastic instability in the weakening of texture therefore partly requires a study of the orientation dependence of PLC effect. Very few studies aimed at understanding this dependence exist. Moreover, these experimental efforts have mostly focussed on the influence of sample orientation on the phenomenon in Al alloys. For instance, Cheng and Morris [11], observed strong anisotropy of the intensity of the PLC effect in a cold drawn Al–Mg based alloy. They showed that the average magnitude of the stress drops,  $\Delta\sigma$ , in the traverse direction (TD) of the alloy were over 70% higher than those in the rolling direction (RD). Similar investigations were also carried out on Al–Li and Al–Cu based alloys, but these results are complicated by the presence of precipitates, which align along specific crystallographic planes making it difficult to determine the influence of sample orientation on the PLC effect [12][13].

While these investigations have provided some insight into the influence of anisotropy on the PLC effect, they do not provide sound mechanistic explanations for the observations made. We argue that direct measurements of the response of single crystals during uniaxial testing is essential for accurate characterization and understanding of the effect of anisotropy on the phenomenon. Yet, such an endeavour is limited by the difficulty of producing bulk single crystals of technical alloys. One way to circumvent this difficulty is to test single grains of alloys that exhibit the PLC-type plastic instability. An attempt was made in this regard by Kovács et. al. [14]; they found that plastic instabilities were more pronounced when the diagonal of a Vickers microindenter coincided with the  $\langle 110 \rangle$  crystal direction in  $\langle 100 \rangle$ -oriented grains in an Al–Zn–Mg–Cu alloy. They hypothesized that the instabilities are enhanced because multiple slip only occurs in this configuration. However, FCC crystals are known to be isotropic especially when indented with pyramidal shaped indenters. Hence, the microscopic origin of the observed orientation dependence is not clear.

In the present study, we gained insight into the microscopic origin and anisotropy of plastic instability in Mg alloys, using a combination of spherical nanoindentation of single grains of Mg alloy AZ91 and local orientation image measurement (OIM) analysis, while a CPFEM model was used to quantify the distribution of slip activities as a function of orientation. By considering the orientation dependence of the difference in shear stress,  $\Delta\tau$ , between consecutive displacement burst events, the anisotropy of the PLC effect was identified. Moreover, the activation volume and energies for the PLC effect were accessed by a statistical analysis of these stress jumps,  $\Delta\tau$ . Finally, on the basis of information garnered from the preceding methods and analysis, we presented a mechanistically sound model for the origin and anisotropy of PLC effect in solution strengthened Mg alloys tested under similar conditions.

## 2 Materials, methods and numerical procedures

### 2.1 Mg alloy AZ91 and pure Mg

The magnesium alloy AZ91 with measured composition in wt.% of 8.58Al–0.65Zn–0.16Mn was chosen for this investigation because it displays PLC–type plastic instability during room temperature deformation [15], unlike the Mg–RE alloys which only exhibit the phenomenon at elevated temperatures. Testing at ambient temperatures simplifies the analysis since mechanisms such as dynamic recrystallization and the increased non-basal slip activities observed during elevated temperature deformation are circumvented. Since the plastic instabilities observed in nanoindentation of pure Mg are associated with the mechanisms other than PLC effect [16], we tested a 99.85% pure Mg alloy to benchmark the instabilities observed in pure Mg against those in the AZ91 alloy. Both the pure Mg and AZ91 were heat treated in an argon protected furnace held at 350 °C for 24 and 48 hours, respectively, and then water quenched. This treatment resulted in extensive grain growth and the near complete dissolution of the  $\beta$ –phase ( $\text{Mg}_{17}\text{Al}_{12}$ ) that forms as precipitates in the Mg–Al–Zn alloys. The ~1mm diameter sized grains obtained provided sufficient area for arrays of nanoindents to be made faraway from grain boundaries.

### 2.2 Methods

The samples used for the investigation were mechanically ground and polished using standard metallography procedures. Four grains with index planes close to (0001) basal,  $\{10\bar{1}0\}$  prismatic,  $\{2\bar{1}\bar{1}0\}$  pyramidal and the  $\{10\bar{1}2\}$  easy glide planes, were identified in each of the samples, i.e., pure Mg and AZ91, using electron backscatter diffraction (EBSD). The  $\{10\bar{1}2\}$  easy glide plane is so called because basal slip has the highest Schmid factor in this orientation. Representations of the investigated crystal orientations in the AZ91 sample and their respective positions in an IPF map are shown in Fig. 1. The angle,  $\Phi$ , between the plane normal

to these orientations and the  $c$ -axis are also shown in Fig. 1. Very similar orientations were also tested in the pure Mg sample.

Nanoindentation tests were performed using a Nanoindenter XP (MTS Corp.) fitted with a spherical diamond indenter with a  $10\mu\text{m}$  radius, and using the CSM (continuous stiffness measurement) mode. 15 indents were carried out in each grain, using constant strain rate of  $0.005\text{s}^{-1}$  to a depth of  $2\mu\text{m}$ . In order to investigate the possible nSRS, strain rate jump tests were also performed using 4 different rates that range from a base strain rate of  $0.05\text{ s}^{-1}$  to  $0.0005\text{ s}^{-1}$ .

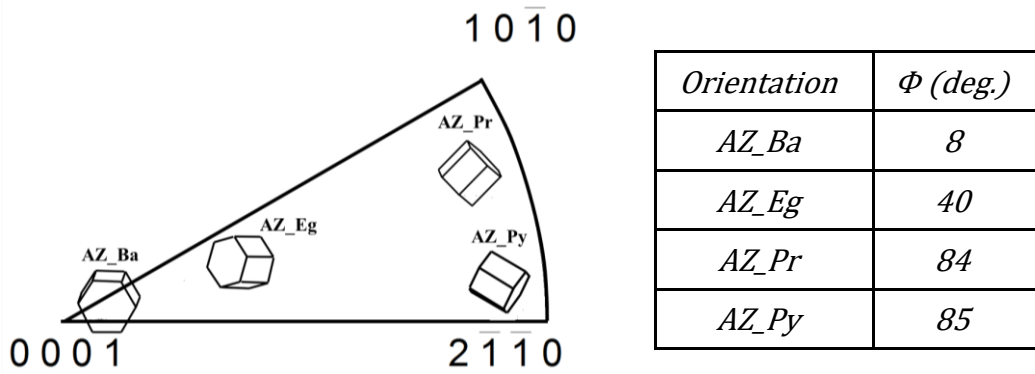


Fig. 1: Schematic of the investigated crystal orientations in the AZ91 sample and their respective positions in an inverse pole figure (IPF).  $\Phi$  is the angle between the plane normal to these orientations and the  $c$ -axis of the HCP crystal.

Following nanoindentation, the deformation characteristics, i.e. slip and twinning, were analysed with a combination of SEM imaging and EBSD measurements performed at the surface as well as on cross sections of the indents. Cross sectioning through the indents were done along two different orientations in order to more accurately capture the anisotropy of the deformation characteristics. The cross sections, with widths of  $\sim 2\mu\text{m}$ , were cut out of the middle section of the indent using focussed ( $\text{Ga}^+$ ) ion beam (FIB) and then attached to a TEM Cu-grid with a micromanipulator. EBSD scans were afterwards performed at 15kV with a step size of 100nm to ensure that detailed information about the microstructure was captured.

### 2.3 Crystal plasticity finite element method (CPFEM)

Finite element simulations of the indentation process were conducted within a crystal plasticity framework to access the relative slip activity on different slip systems in the indented grains. The framework is based on the commonly used concept of elasto-viscoplastic deformation along discrete (slip) planes, which goes back to the work of Rice [17], Peirce et al. [18] and Asaro [19]. In this framework, the Cauchy stress tensor is projected on individual slip planes by the Schmid tensor, representing the elementary deformation systems. The strain rate  $\dot{\gamma}$  of the system  $\alpha$  is given by a visco-plastic power law constitutive formulation [18]:

$$\frac{\dot{\gamma}^{(\alpha)}}{\dot{\gamma}_0^{(\alpha)}} = \left| \frac{\tau^{(\alpha)}}{\tau_y^{(\alpha)}} \right|^n \text{sign} \left( \frac{\tau^{(\alpha)}}{\tau_y^{(\alpha)}} \right), \quad (1)$$

where  $\dot{\gamma}^{(\alpha)}$ ,  $\dot{\gamma}_0^{(\alpha)}$ ,  $\tau^{(\alpha)}$  and  $\tau_y^{(\alpha)}$  are the slip rate, reference strain rate, resolved shear stress and the current strength of the  $\alpha$  slip system, respectively. The power exponent,  $n$ , is the strain rate sensitivity parameter.

It has been previously shown that four families of deformation modes, including the 3 basal  $\langle a \rangle$ , 3 prismatic  $\langle a \rangle$ , 6 pyramidal  $\langle a + c \rangle$  slip and the  $\{10\bar{1}2\}$  tensile twinning systems suffice to reproduce the mechanical behaviour of magnesium single- and polycrystals during channel die experiments [20]. This same set of systems was used here. It should be noted that the CPFEM framework does not explicitly account for the crystal reorientation that physically results from twinning. Rather, it allows the twinning strain to saturate and then applies a hardening function, which significantly increases the strength of the twinning system after a critical strain is reached [20]. Hence, no additional slip or twinning is allowed in the twinned region.

The evolution equation of the slip strengths,  $\dot{\tau}_y^{(\alpha)}$ , after activation of slip is governed by:

$$\dot{\tau}_y^{(\alpha)} = \sum_{\beta} h_{\alpha\beta}(\bar{\gamma}) \dot{\gamma}^{(\alpha)}, \quad (2)$$

where  $\bar{\gamma}$  and  $h_{\alpha\beta}$  are the cumulative shear strain on all slip systems and the strain hardening parameter, respectively. The latter is assumed to be composed of a self-hardening contribution which is given as:

$$h_{\alpha\alpha} = h(\bar{\gamma}) \quad (3)$$

and a latent-hardening contribution:

$$h_{\alpha\beta, \alpha \neq \beta} = q_{\alpha\beta} h(\bar{\gamma}), \quad (4)$$

where the interaction parameter,  $q_{\alpha\beta}$ , accounts for the interaction between families of active slip systems. Moreover, the self-hardening contribution consists of three different hardening laws, namely, a linear hardening, Voce hardening and a hardening law that captures the sudden stress increase that arises when twinning saturates. Both the self- and latent-hardening parameters were previously calibrated by Graff et. al [20] by fitting them against experimental results from single- and poly-crystalline channel die tests. These parameters are presented in Tables S1 and S2 of the supplementary material to this paper.

The indented grains were modelled as a cylindrical block of material, discretised by 20,000 linear 8-noded solid elements. The radius,  $r$ , and height,  $h$ , of the cylinder are chosen large enough that strain imposed from the indentation is close to zero at its boundaries:  $r/r_i = 3$  and  $h/r_i = 3$ , with  $r_i$  being the radius of the indenter. The indenter was modelled as rigid surface contacting the substrate, see Fig. 2. For each orientation considered, one simulation under displacement control of the indenter was conducted up to a normalised penetration depth of  $h/r_i = 0.2$  over 100 seconds; this leads to a strain rate of  $0.002\text{s}^{-1}$ . The orientation of the

respective grain was mapped to the simulation by prescribing the experimentally measured Euler angles. The simulations were performed using the implicit FE-code ABAQUS together with a user material subroutine (UMAT) [21][22]. Isotropic elasticity, with Young's modulus,  $G$ , of 45GPa and Poisson ratio,  $\nu$ , of 0.3 were assumed for the simulations. The simulations were performed under quasi-static loading conditions, with a strain rate sensitivity parameter set to 30. As a result, the simulation results can be considered to be rate independent. The accumulated shear strain is evaluated for each family of slip and twinning system,  $\alpha$ , as the integral over time of Eqn. (1). The accumulated slip activity is given as the ratio of strain of a system over total strain, and is calculated in order to assess the contributions of each deformation system to the overall deformation.

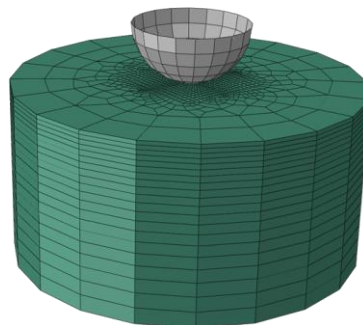


Fig. 2: Finite element model of the bulk material (cylinder) and the indenter (rigid sphere)

Although the material parameters used for the simulations are those of pure Mg, the orientation used in the simulations are the actual Euler angles of the investigated grains in the AZ91 sample. Furthermore, although the absolute value of critical resolved shear stress (CRSS) on each slip system will be different in pure Mg and AZ91, it has been shown that that Al and Zn atoms do not alter the slip or twinning systems that are activated during deformation [23][24][25][26].

### 3 Results and data analysis

#### 3.1 Nanoindentation results

The load ( $P$ ) vs. displacement ( $h$ ) response of tests conducted under constant strain rate conditions in single grains of the AZ91 and pure Mg samples with orientations close to the pyramidal planes, i.e. AZ\_Py and PM\_Py, are shown in Fig. 3(a) and (b), respectively. Only sections of the curves are shown in order to reveal salient details. Displacement bursts, which are an indication of the presence of some sort of plastic instability, occur in both samples. However, the displacement bursts are more ubiquitous and significantly smaller in magnitude ( $\Delta h$ ) in the alloy. We would argue that these are associated with PLC-type plastic instability. Moreover, similar behaviour has been observed in Al–Li and Al–Mg based alloys where twinning is absent [27]. A few displacement bursts with significantly large magnitudes,  $\Delta h$ , were also observed in the AZ91 samples. These are analogous to the burst events in the pure Mg sample and are most likely associated with the nucleation and growth of twins [16] or non-PLC type dislocation avalanches often observed in relatively pristine single crystals

Strain rate jump tests were also conducted in both samples to further confirm the presence or absence of PLC-type plastic instability. A section of the  $P$  vs.  $h$  curve that shows the response which accompanies the change in nanoindentation strain rate between a strain rate of 0.0005/s ( $\dot{\epsilon}_2$ ) and the base strain rate, 0.05/s ( $\dot{\epsilon}_1$ ), is shown in Fig. 3(c) and (d) for AZ91 and pure Mg, respectively. An increase in load is observed in the alloy as the strain rate is decreased from  $\dot{\epsilon}_1$  to  $\dot{\epsilon}_2$ , while a decrease in load is observed in pure Mg when  $\dot{\epsilon}_1$  is decreased to  $\dot{\epsilon}_2$ . The response of the alloy and the pure Mg sample is indicative of nSRS and positive strain rate sensitivity, respectively. We can thus confirm that the displacement bursts observed in the AZ91 sample are largely as a result of the operation of the underlying mechanism(s) that govern the PLC effect.

Displacement bursts characteristic of the PLC effect were observed in all four investigated grains of the AZ91 samples. Representative  $P$  vs.  $h$  curves of the indents are shown in Fig. 4(a). The anisotropy of the displacement burst events is however not directly apparent in the curves. What is rather observed is a slight influence on the  $P$  vs.  $h$  response. This is more clearly shown in Fig. 4(b) where the average  $P$  vs.  $h$  response of all 15 indents in each of the four different grains, along with the associated standard deviations, is plotted.

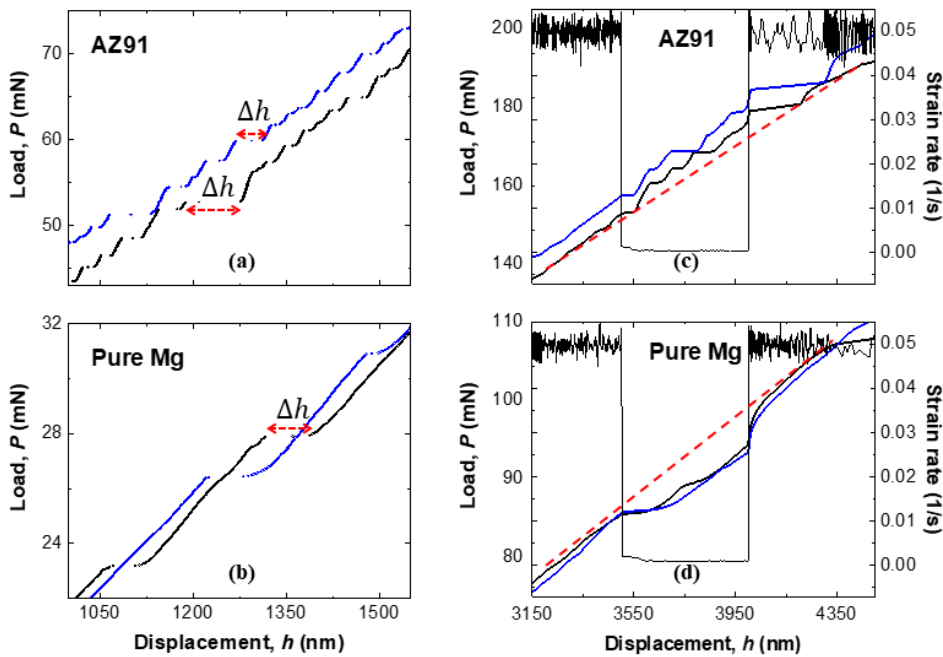


Fig. 3: A section of two individual (in back and blue) load ( $P$ ) vs. displacement ( $h$ ) curves for (a) AZ91 and (b) pure Mg conducted under constant strain rate conditions.  $\Delta h$  is the magnitude of the displacement burst. The displacement bursts are more prevalent, smaller and regular in the alloy. Sections of the  $P$  vs.  $h$  response from strain rate jump tests for (c) AZ91 and (d) pure Mg are also plotted. The broken red lines are guides for the eye.

In order to characterise the anisotropy of the PLC effect, we note that each displacement burst event is indicative of a rapid release of mobile dislocations from obstacles where they have been temporarily locked. We will name the local maximum load that precedes a displacement burst as the “release” load while the load at the end of such an event will be called the “arrest” load. Data points corresponding to the “release” and “arrest” loads are highlighted

in Fig. 4(a) with black open squares and circles, respectively. These data points were identified in Python with a script that determines local maxima and minima points in the displacement rate data and gives the corresponding load, displacement and harmonic contact stiffness values. Only data points above a displacement of 500nm, beyond which the displacement bursts were unambiguously delineated, were considered. Moreover, we define  $\Delta P$  as the difference between the release and arrest loads.  $\Delta P$  is proportional to the additional shear stress,  $\Delta\tau$ , required to release the solute decorated mobile dislocations from the solute clustered forest dislocations where they have been trapped, while  $\Delta h$  is equivalent to the shear strain produced by this additional shear stress.  $\Delta P$ , and by extension  $\Delta\tau$ , will be equal to zero in the absence of the underlying micromechanisms that govern the PLC effect. It has been shown that  $\Delta\tau$ , which is also known as the break-free stress, is material-, strain rate-, temperature- and dislocation density-dependent [11][27][28][29][30].

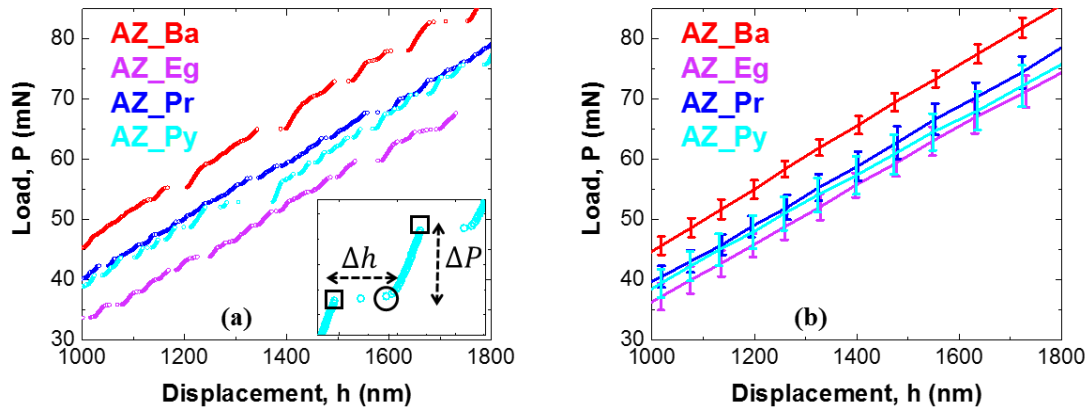


Fig. 4: Representative load ( $P$ ) vs. displacement ( $h$ ) curves (a) and Average  $P$  vs.  $h$  response with the corresponding standard deviations (b) of indents made in the investigated orientations. In the insert in (a), data points corresponding to the “release” load are highlighted with black open squares, while the black open circle shows a data point corresponding to an “arrest” load.  $\Delta P$  is the magnitude of the load difference between corresponding displacement burst events, while  $\Delta h$  is the displacement burst size.

In this work, we relate  $\Delta P$  to  $\Delta\tau$  with the relation:

$$\frac{MC^*\Delta PE_r^2}{S^2} = \Delta H = 3\sqrt{3}\Delta\tau, \quad (5)$$

Where  $M$  is the indentation Schmid factor (ISF),  $C^*$  is a constant,  $E_r$  is the reduced modulus – assumed to be 47GPa in this work,  $S$  is the harmonic contact stiffness and  $\Delta H$  is the difference in hardness between consecutive displacement burst events. The ISFs for basal, prismatic and pyramidal slip systems Mg have been numerically computed by Zhang et. al.[31] and are presented in Fig. S1 of the supplementary material. We note however, that only the ISFs for basal slip were utilized since, as later discussed in section 4,  $\Delta P$  and consequently  $\Delta\tau$ , is largely governed by basal slip activity. The contact stiffness rather than contact area was used in the analysis because the morphology of the indents, especially those in the prismatic and pyramidal planes, were not spherical but elliptical. The conventional relationship for computing indentation contact area breaks down in such conditions. A plot of  $\Delta\tau$  vs.  $h$  for a single indent in AZ\_Eg and AZ\_Pr is shown in Fig. 5(a). Only  $\Delta\tau$  values that lie within the range:  $\overline{\Delta\tau} \pm SD$ , where  $\overline{\Delta\tau}$  and SD are the average and standard deviation, respectively, were considered. This simple approach was adopted in order to minimize the possibility of including  $\Delta\tau$  values related to noise and other non-PLC mediated instabilities. We would argue that this is a reasonable approach, especially with regards to twinning, since  $\Delta\tau$  for twinning events are larger than those arising from PLC – compare Fig. 3(a) & (b).

Although the  $\Delta\tau$  values, see Fig. 5 (a), are still quite stochastic, it can be argued that the  $\Delta\tau$  values for AZ\_Eg are on average higher than those of AZ\_Pr. We will argue further that the stochasticity most likely arises from local microstructural variations within the grains. This should not be unexpected in a technical alloy such as used in this work. Nevertheless, hidden order have been shown to exist even behind these kinds of stochastic behaviour, and cumulative

statistics, because of its superiority in providing unbiased comparison of data sets, have been shown to be a useful tool for revealing these hidden orders [27][32][33][34]. This approach is also adopted in this work and a plot of the cumulative distribution (CDF) of  $\Delta\tau$  as a function of crystal orientation is shown in Fig. 5 (b). Each curve in the figure consists of between 300 and 650  $\Delta\tau$  values, from 15 indents at each orientation, and can therefore be considered statistically significant (compare Refs. [33][34][35][36]) and representative of the anisotropy of the PLC effect in AZ91 as can be observed from spherical nanoindentation. Two different trends are clearly identifiable from Fig. 5(b); the prismatic and pyramidal planes, i.e. AZ\_Pr and AZ\_Py, show very similar response and are more deterministic than AZ\_Ba and AZ\_Eg, where larger scatter is observed. Moreover, the average values of  $\Delta\tau$  obtained in AZ\_Ba and AZ\_Eg ( $1.00\pm 0.4$  and  $1.84\pm 0.8$  MPa, respectively) are at least 50% higher than those obtained in AZ\_Pr and AZ\_Py ( $0.56\pm 0.2$  and  $0.67\pm 0.2$  MPa, respectively). This behaviour is a strong indication that the additional shear stress,  $\Delta\tau$ , required to release the trapped mobile dislocations is also orientation dependent. Interestingly, the orientation dependence of  $\Delta\tau$  (Fig. 5b) is more pronounced than that of the global strength,  $\tau$  ( $\tau \propto P$  in Fig. 4). It is also notable that the orientation dependence of  $\tau$  and  $\Delta\tau$  are reversed: the highest  $\Delta\tau$  and the lowest  $\tau$  values were exhibited in the AZ\_Eg orientation, an indication that the origin of the orientation dependence in the two cases is different.

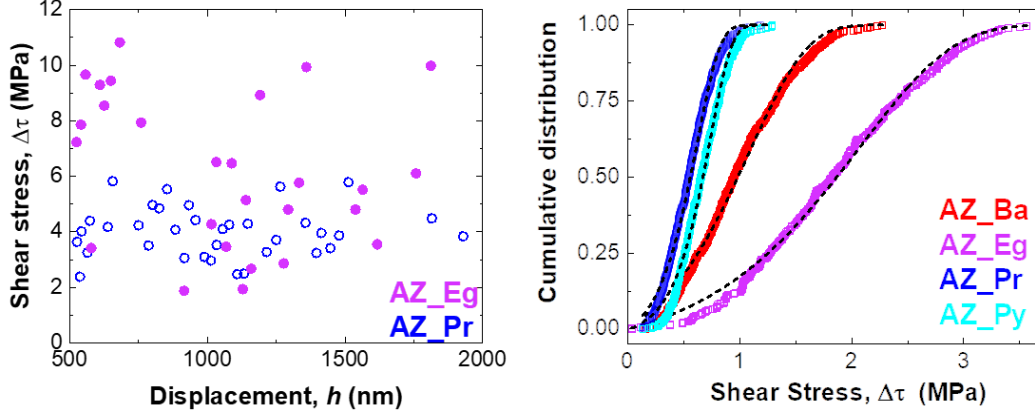


Fig. 5: (a) Shear stress between consecutive displacement bursts,  $\Delta\tau$ , for single tests in AZ\_Eg and AZ\_Pr plotted against displacement,  $h$ . (b) Cumulative distribution of  $\Delta\tau$  plotted as a function of the indented plane (orientation). The black dotted lines are fits of the statistical thermal activation model presented in Eqn. (9).

### 3.2 Activation parameters for PLC-type plastic instability

In order to estimate the activation volume and activation energy for PLC-type plastic instability from the cumulative distribution data presented in Fig. 5, we adopted a modified version of the statistical thermal activation model originally proposed by Schuh and Lund [33] for extracting activation parameters from incipient plasticity data. These authors show that the local rate,  $\dot{N}$ , at which displacement bursts (dislocations nucleation) arising from incipient plasticity occurs can be described by [33]:

$$\dot{N} = \eta \exp\left(-\frac{\Delta H - \tau^* v^*}{kT}\right), \quad (6)$$

where  $\eta$  is the attempt frequency,  $\Delta H$  is the activation enthalpy,  $\tau^*$  is the local shear stress,  $v^*$  is the activation volume and  $kT$  is the thermal energy. Since PLC-type plastic instability is also marked by the thermally activated release of dislocations from their pinned positions, it can likewise be described by such a formulation. We only note that the local shear stress term,  $\tau^*$ , in Eqn. (6) is replaced by  $\Delta\tau$ , which is the local shear stress associated with the PLC effect.  $\Delta\tau$  depends on the current time, the time at which the dislocation become pinned at the current

obstacle and the time dependent backstress exerted on the pinned dislocations by the solute decorated forest dislocations [6]. Moreover, it has been shown that essentially all the plastic strain experienced during the nanoindentation of materials exhibiting plastic instability occur during the displacement burst events [37]. It can therefore be assumed that  $\Delta\tau$  is elastic and can be rewritten in terms of the strain rate,  $\dot{\epsilon}$ , and time,  $t$  as follows:

$$\Delta\tau = G\gamma \approx G\dot{\epsilon}t, \quad (7)$$

where  $G$  is the shear modulus and  $\gamma$  is shear strain. Substitution of Eqn. (6) and (7) into the Eqn. (8),

$$F(t) = 1 - \exp\left(-\int_0^t \dot{N}(t')dt'\right), \quad (8)$$

which is the link between the CDF and the local rate,  $\dot{N}$ , at which displacement bursts occurs [41], and integrating yields [42]:

$$F(\tau, T) = 1 - \exp\left(\frac{\eta kT}{G\dot{\epsilon}v^*} \left[ \exp\left(-\frac{\Delta H}{kT}\right) - \exp\left(\frac{v^*\Delta\tau - \Delta H}{kT}\right) \right]\right). \quad (9)$$

A fit of Eqn. (9) to the experimental cumulative distribution of  $\Delta\tau$ , with the constants  $kT=4.11e^{-21}$ J,  $G=17$ GPa and  $\dot{\epsilon}=0.005s^{-1}$ , yields the solution for the parameters,  $v^*$ ,  $\Delta H$  and  $\eta$ . These values are presented in Table 1, while the experimental CDF together with the fitting curve are shown in Fig. 5b.

Table 1: Values of the attempt frequency,  $\eta$ , the activation volume,  $v^*$  and the activation enthalpy,  $\Delta H$ . ' $b$ ' is the burgers vector for basal slip.

	$\eta$ ( $*1e11 s^{-1}$ )	$v^*$ ( $b^3$ )	$\Delta H$ (eV)
<b>AZ_Ba</b>	2.69	445	0.60
<b>AZ_Eg</b>	5.60	277	0.64
<b>AZ_Pr</b>	1.62	1106	0.59
<b>AZ_Py</b>	1.31	1179	0.60

### 3.3 Microstructural analysis

SEM micrographs of indents made in the AZ\_Ba, AZ\_Eg, AZ\_Pr and AZ\_Py planes are shown in Fig. 6(a–d) while IPF maps of cross sections of indents made in each of these orientations are shown in Fig. 6(e–I). Specifically, Fig. 6 (e) and (i) shows cross sections of indents in AZ\_Ba with out-of-plane orientations close to  $\langle 2\bar{1}10 \rangle$  and  $\langle 10\bar{1}0 \rangle$  directions respectively, Fig. 6 (f) and (j) shows cross sections of indents in AZ\_Eg viewed from orientations close to  $\langle 10\bar{1}2 \rangle$  and  $\langle 10\bar{1}0 \rangle$  directions respectively, Fig. 6 (g) and (k) shows cross sections of indents in AZ\_Pr viewed from orientations close to  $\langle 0001 \rangle$  and  $\langle 2\bar{1}10 \rangle$  directions respectively, while Fig. 6(h) and (l) shows cross sections of indents in AZ\_Py viewed from orientations close to  $\langle 0001 \rangle$  and  $\langle 10\bar{1}0 \rangle$  directions respectively.

As indicated earlier, indents made in the AZ\_Ba plane were all spherical in shape and only a very small volume of the matrix near the edge of the indent (see “y” in Fig. 6i) was twinned in this orientation. Moreover no slip activity was visible in the vicinity of the indent since the geometry of the crystal obviates the upward glide of any of the slip systems. The negligible presence of twinning indicates that the deformation in this orientation is slip mediated. In contrast, basal slip activity and twinning were more pronounced in the other three planes, especially in the AZ\_Pr and AZ\_Py planes. Specifically, significant basal slip activity, extending over a distance of 40 $\mu$ m beyond the indents, and large volumes of twins formed beneath the indents made in the AZ\_Pr and AZ\_Py planes (see Fig. 6c–d and g–h). Moreover,

the different variants of twins observed in these maps were all identified as  $\{10\bar{1}2\}$  tensile twins. It is noteworthy that the slip and twinning activities observed in the AZ91 alloy are comparable with those observed in pure Mg single crystals of similar orientations deformed with a 1mm spherical nanoindenter [38]. This further reinforces our view that the active slip and twinning systems are not altered by the presence of Al and Zn atoms.

Further insight into the local deformation characteristics in each indented plane was gained from visual images of the variation of the local misorientations in the vicinity of the indents. These misorientations occur due to geometrically necessary dislocations (GNDs) formed during plastic deformation. The approach used in this work to analyse the local misorientations is the grain reference orientation deviation (GROD) method. In this method, each point indexed during the EBSD scan is coloured according to the misorientation it makes relative to the average orientation of the grain [39].

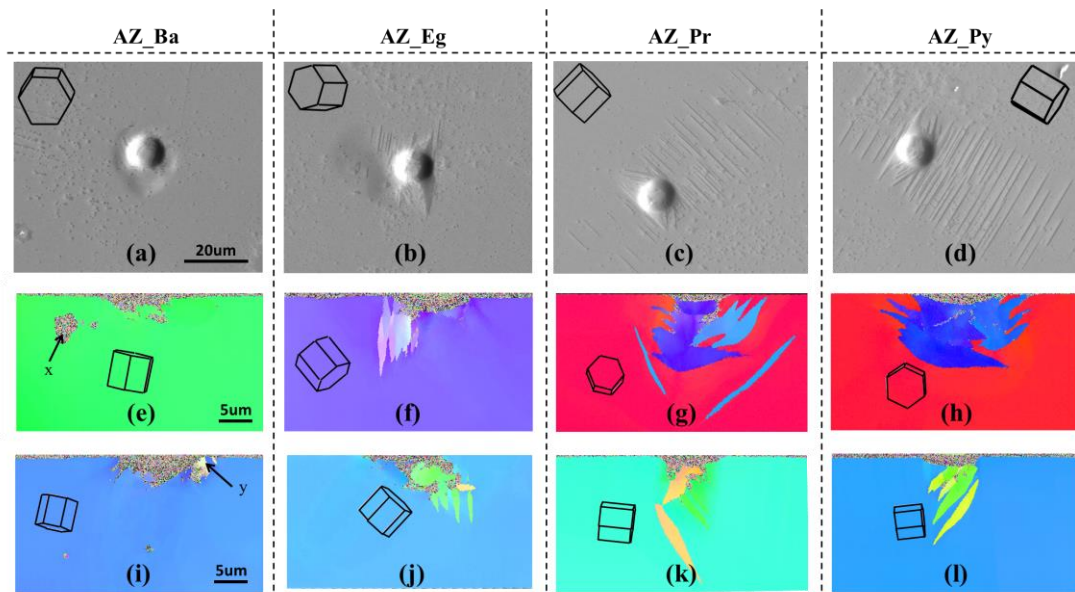


Fig. 6: SEM image of the indents and EBSD IPF maps of cross sections of the indents for all investigated orientations. The cross sections were taken from two different orientations within each indented plane. The marker “x” points to precipitate and marker “y” in (i) points to a twin.

The GROD maps of the SEM images and IPF maps presented in Fig. 6 are shown in Fig. 7(a-l). All twinned areas and badly indexed points were removed prior to the GROD analysis.

It is apparent from these maps (Fig. 6 and Fig. 7) that although the highest degree of misorientation,  $>8^\circ$ , occurred mostly at the interface between twinned and untwinned areas of the crystal (see e.g. Fig. 7f–g), the overall distribution of misorientations around each indent and the resulting accumulated strain from the GNDs are significantly higher in the AZ\_Eg and AZ\_Ba planes in comparison to the AZ\_Pr and AZ\_Py planes. As we will show later, this has implications for the anisotropy of the PLC effect.

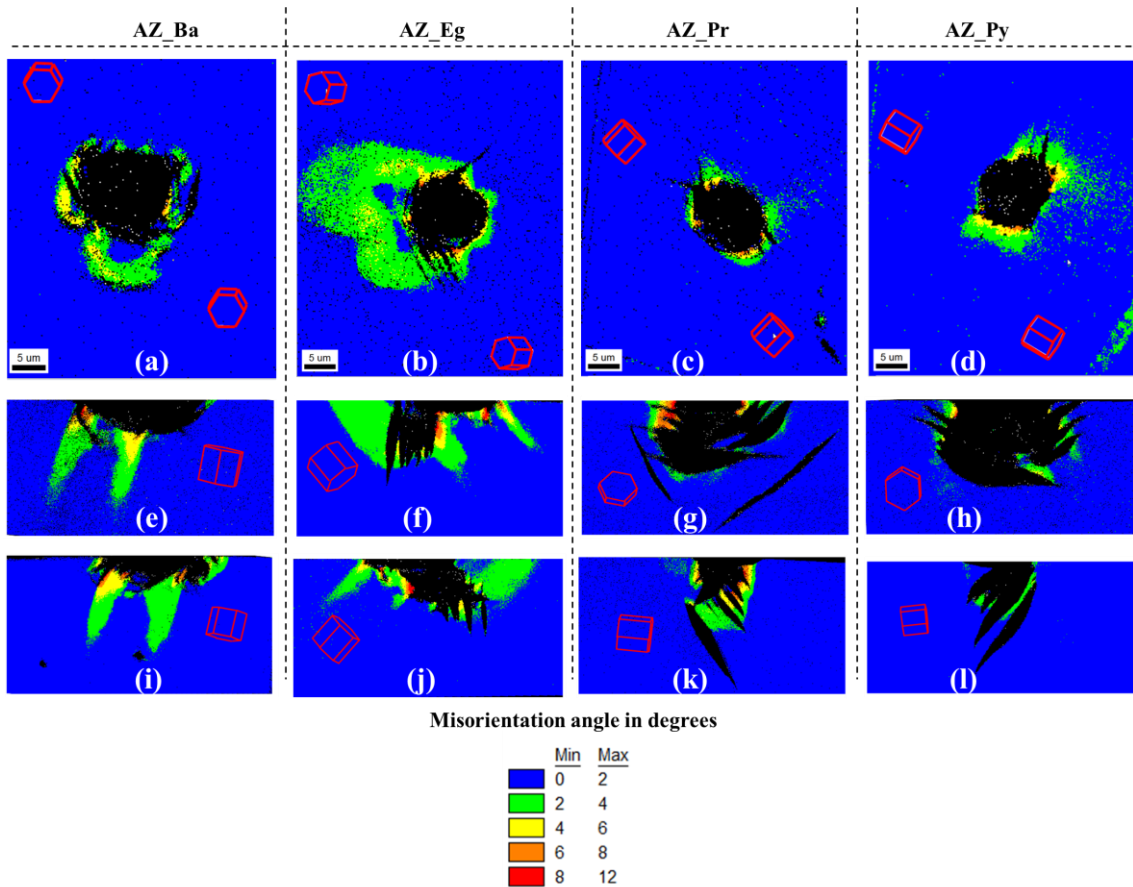


Fig. 7: Grain orientation deviation (GROD) maps of the top surface (a,d,g,h) and cross section of indents made in the investigated orientations. The change in colour from blue to red is indicative of the magnitude of local lattice rotations (in degrees) induced by plastic deformation during the nanoindentation process. Regions in black refer to twins and unidentifiable scan points.

### 3.4 CPFEM identification of relative dislocation distributions

Although the GROD maps are good indicators of the distribution of the local misorientation, and by extension the GNDs, they do not give insight into the active slip systems that give rise

to the observed misorientation. Such information is crucial to understanding the orientation dependence of  $\Delta\tau$ , and can be assessed from the CPFEM results.

The accumulated activity of the basal, prismatic, pyramidal II and twinning systems in each of the investigated orientations are shown in Fig. 8(a–p). Fig. 8(a–d) shows that there is very high activity of basal slip in all four orientations. This behaviour is expected because of the interplay between the multi-axial stress state imposed by the indenter and the low CRSS of the basal plane. Prismatic slip activity is also observed in all four orientations, see Fig. 8(e–h). Moreover, the simulations show that the activity of pyramidal slip, Fig. 8(i–l), is significantly larger in the AZ\_Ba and AZ\_Eg planes in comparison to its activity in the AZ\_Pr and AZ\_Py planes. It is noteworthy that the basal and pyramidal slip systems are confined to the same regions in the AZ\_Ba and AZ\_Eg orientations; with each of slip system contributing roughly 50% of the deformation in these localised regions. The simulations also show that twinning activity, shown in Fig. 8(m–p), is negligible in AZ\_Ba but significant in the other 3 orientations. The simulated twinning activity is thus very consistent with the EBSD analysis reported in section 3.3. We also note that in general, there is good agreement between the CPFEM analysis presented here and other studies of single crystalline pure Mg of similar orientations [38][40]. Moreover, the simulated load vs. displacement curves,  $P_{sim}$  vs.  $h_{sim}$ , and those of the pure Mg sample are also in good agreement. These plots are shown in Fig. S2 of the supplementary material.

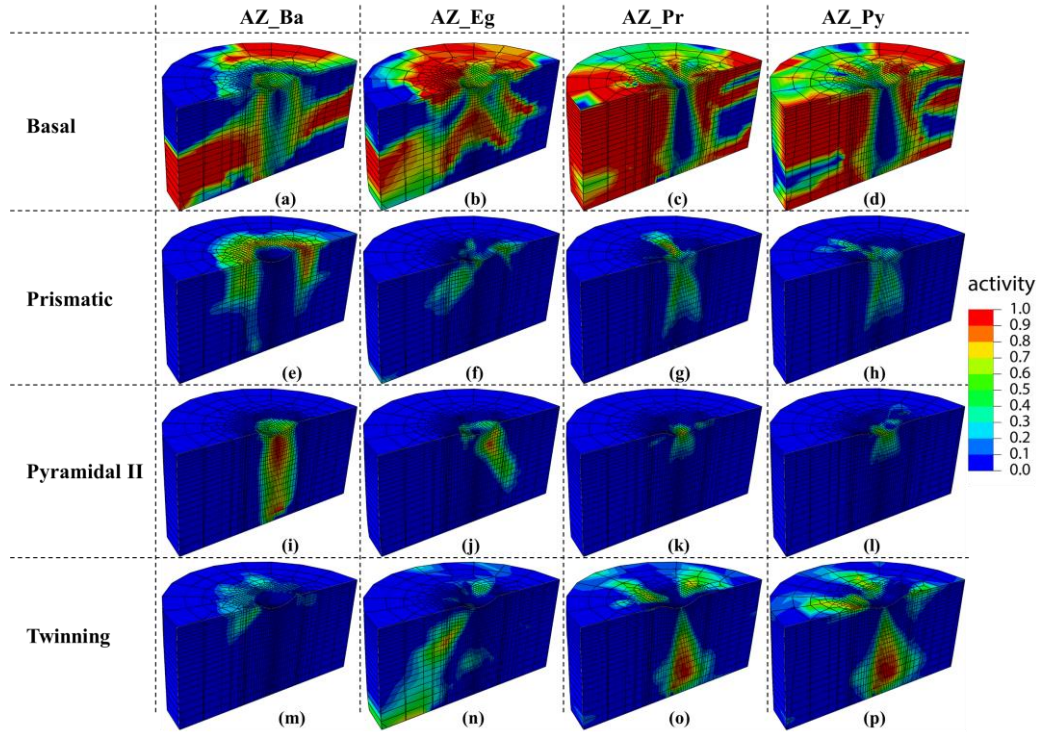


Fig. 8: Relative activity of slip/twinning in AZ\_Ba, AZ\_Eg, AZ\_Pr and AZ\_Py.

#### 4 Discussion

The preceding results and analysis clearly point to the occurrence of two levels of anisotropy, namely, a slight orientation dependence of the global  $P$  vs.  $h$  response (Fig. 4) and a more significant dependence of  $\Delta\tau$  on orientation (Fig. 5b). Specifically, Fig. 4 shows that AZ\_Ba with angle  $\Phi=8^\circ$ , i.e. with loading axis almost parallel to C-axis, attained the highest load, as is the case for for uniaxial testing, while AZ\_Eg ( $\Phi=40^\circ$ ), which is close to the configuration where basal slip has the highest (uniaxial) Schmid factor, attained the lowest load. Moreover, both microstructural (Fig. 6) and CPFEM (Fig. 8) analysis show negligible twinning in AZ\_Ba as is the case for uniaxial microcompression of pure Mg (0001) single crystal [43]. These indicate that the observed orientation dependence of the global  $P$  vs.  $h$ , is still largely governed by the resolved shear stress (RSS) on the most favourably oriented slip system, but to a lesser extent than obtained during uniaxial testing.

#### 4.1 *Micromechanisms underlying PLC effect in Mg AZ91*

The anisotropy of the PLC effect is inherently coupled to its underlying microscopic mechanisms. The experimental and numerical analyses presented herein indicate that the PLC effect is not twin mediated as suggested by Li et. al. [47] for Mg-Li-Al-Zn-Re. That the highest  $\Delta\tau$  values occur both in the near-absence (AZ\_Ba) and in the presence of twinning (AZ\_Eg), demonstrate that twinning has negligible influence on the magnitude of  $\Delta\tau$  and hence on the PLC effect. Corby et. al. [15] proposed two possible mechanisms, a non-diffusional and a diffusional model, for PLC effect in AZ91. The non-diffusional model cannot apply here since nSRS, as observed in this work, see Fig. 3c, is known to be diffusion mediated [3][6][7]. In the diffusional model, they propose that PLC is governed by the classical dynamic strain aging (DSA) model, i.e. the dynamic interaction of solute atoms with dislocations temporarily trapped by forest dislocations, consistent with studies on other Mg alloys [44][45][46]. More specifically, they suggest that Al atoms, being lighter and hence more mobile than Zn atoms, will be the dominant aging species, while Zn lowers the critical stress for cross slip from the basal to the prismatic planes and thus facilitates the formation of dislocation forest on the latter. The microstructural and CPFEM analysis conducted in this work along with recent analytical models and density function theory (DFT) based calculations by other workers [6][24][48][49] however suggest that the diffusional model of Corby et. al. [15] is implausible for the following reasons. Firstly, it has been shown DSA cannot independently lead to nSRS [49]. As previously discussed, solute aging of the forest dislocations is an additional requirement, especially in solution strengthened alloys. Secondly, the CPFEM analysis in Fig. 8(e-h) shows that the prismatic slip activity is minimal in easy glide orientation (i.e AZ\_Eg) yet this orientation has the highest  $\Delta\tau$ . This suggests that prismatic slip has little or influence on the PLC effect. This thesis is further corroborated by molecular dynamics simulations carried out by Yi [50] and Wu [51]. Yi et. al. [50] show that alternating cross slip of  $\langle a \rangle$  dislocations between prismatic and

basal planes occurs unhindered in Mg in the presence of Al and Zn atoms, and this leads to a softening, not hardening of prismatic slip [23][50]. It has also been shown that when activated, there is fast transition of the  $\langle c + a \rangle$  dislocations on the pyramidal II systems to the basal planes where they dissociate and become immobile, invariably increasing the forest density in the basal planes and hindering subsequent glide of dislocations on all slip systems [51]. In other words, forest dislocations are expected to form in the basal planes not in the prismatic planes. Lastly, DFT calculations [52] show, contrary to the view of Corby et. al. [15], that Zn actually diffuses faster than Al in Mg.

Following the breakdown of the preceding models, we now propose a more physically sound mechanistic model for the PLC in Mg alloy AZ91. An underlying premise in this model is that the mechanism is thermally activated and is associated with the main strengthening mechanisms of the alloy, namely solute and forest strengthening. We thus propose that the PLC-type plastic instability in Mg alloy AZ91 is governed by a combination of solute aging of the temporarily trapped mobile dislocations and the solute aging of the forest dislocations [6]. The experimentally determined activation enthalpies (see Table 1) are in very good agreement with DFT calculated values (0.60–0.65eV) for vacancy-mediated pipe diffusion of Al in Mg [52]. This suggests that the solute aging (diffusion) process is largely governed by the vacancy-mediated pipe diffusion of Al atoms. Moreover, the estimated activation volumes (see Table 1) are of the order of  $100b^3$ , a value consistent with some form of dislocation–point defect interaction [1]. However, we note that binary Mg-Al alloys [23] do not exhibit PLC effect, implying that Zn also plays an important role in the occurrence of the phenomenon. We argue, based on DFT calculations by Yasi et. al. [25], that Zn atoms indirectly aid the PLC phenomenon by promoting the formation of dislocation forests on the basal plane. Yasi et. al. [25] show that the constriction of screw dislocations in Mg and the resulting cross slip is aided by atom species with a positive chemical misfit like Zn. Al has a negative chemical misfit.

#### 4.2 *Origin of the anisotropy of PLC effect in Mg AZ91*

It follows from the preceding analysis that the anisotropy of the PLC effect directly results from variations in the density and strength of the forest dislocations in the basal planes. These variations are in turn influenced by the initial orientation of the crystal. This is supported by the GROD maps in Fig. 7, which show that the distribution of misorientations and hence GNDs in AZ\_Eg and AZ\_Ba is significantly larger than in AZ\_Pr and AZ\_Py. Since the presence of GNDs generally leads to an acceleration of the rate of accumulation of statistically stored dislocations (SSDs) [53], we argue that the density of SSDs will be highest in AZ\_Eg followed by the AZ\_Ba, while it will be similar in AZ\_Pr and AZ\_Py. Moreover, the CPFEM clearly shows that the activity of pyramidal II slip is highest in AZ\_Ba and AZ\_Eg. As discussed previously, the  $\langle c + a \rangle$  dislocations on the pyramidal II systems cross slip onto the basal planes where they dissociate and form forest dislocations [51]. Although the CPFEM framework used in this work is unable to capture such mechanisms, the fact that the activity of pyramidal II slip is highest in AZ\_Ba and AZ\_Eg strongly suggest that a correspondingly higher density of dissociated and immobile  $\langle c + a \rangle$  dislocations will be transmitted to and formed on the basal planes in AZ\_Ba and AZ\_Eg than in AZ\_Pr and AZ\_Py. Furthermore, since the strength of the forests scales with both forest density and the concentration of the solutes decorating the forests, we would expect that orientations with high density of forest dislocations would also show more pronounced PLC effect. This is very consistent with observations made in this work. Orientations AZ\_Eg and AZ\_Ba which apparently show higher density of forest dislocations have more pronounced instabilities than AZ\_Pr and AZ\_Py (compare Fig. 5b and Fig. 7).

### 5 **Conclusion**

Insight into the influence of PLC-type plastic instability on texture weakening requires an understanding of the underlying mechanisms that govern PLC and the orientation dependence of the phenomenon in a single crystal. Based on the experimental and theoretical analysis

carried out on single grains of Mg AZ91, we show that the PLC effect in Mg AZ91 originates from the aging of temporarily trapped mobile dislocations and forest dislocations by Al atoms. We argue that Zn atoms indirectly aid the PLC effect by facilitating the formation of forest dislocations on the basal planes. Moreover, our results also reveal a strong correlation between the density of forest dislocations and crystallographic orientation. Specifically, orientations with high activity of pyramidal II  $\langle c + a \rangle$  slip enhance forest dislocation density. The PLC effect is more pronounced in such orientations since the strength of the forest dislocations scales with the dislocation density and the amount of solute, i.e., Al, that decorates the forest.

These results have strong implications on texture weakening. In particular, since the PLC-mediated strength increase in the basal plane facilitates the activation of other non-basal slip systems it leads to a decrease in basal texture. It should therefore follow that solutes that strongly promote the formation of forest dislocations in the basal planes and the dynamic strain aging of temporarily trapped mobile dislocations and dislocations forests in Mg-based alloys would exhibit weakened texture and consequently improved formability.

## 6 References

- [1] A.G. Evans, R.D. Rawlings, The thermally activated deformation of crystalline materials, *Phys. Stat. Sol.* 34 (1969) 9–31.
- [2] R. Li, R.C. Picu, J. Weiss, Dynamics below the depinning transition of interacting dislocations moving over fields of obstacles, *Phys. Rev. E* 82 (2010) 022107-1.
- [3] H. Ovri, E.T. Lilleodden, New insights into plastic instability in precipitation strengthened Al-Li alloys, *Acta Mater.* 89 (2015) 88-97.
- [4] A. Yilmaz, The Portevin-Le Chatelier effect: a review of experimental findings, *Sci. Tech. of Adv. Mater.* 12 (2011) 063001.
- [5] W.A. Curtin, D.L. Olmsted, L.G. Hector Jr., A predictive mechanism for dynamic strain ageing in aluminium–magnesium alloys *Nat. Mater.* 5 (2006) 875–880.
- [6] M.A. Soare, W.A. Curtin, Solute strengthening of both mobile and forest dislocations: the origin of dynamic strain aging in FCC metals, *Acta Mater.* 56 (2008) 4046–4061.
- [7] E. Rizzi, P. Hähner, On the Portevin–Le Chatelier effect: theoretical modelling and numerical results, *Intl. J. of Plast.* 20 (2004) 121–165.
- [8] L. Jiang, J.J. Jonas, R.K. Mishra, Dynamic strain aging behaviour of a Mg-Ce alloy and its implications for extrusion, *Mater. Sci. Forum* 706-709 (2012) 1193–1198.
- [9] L.W.F. Mackenzie, M.O. Pekguleryuz, The recrystallization and texture of magnesium-zinc-cerium alloys, *Scr. Mater.* 59 (2008) 665–668.
- [10] T. Wang, L. Jiang, R.K. Mishra, J.J. Jonas, Effect of Ca addition on the intensity of rare earth texture in extruded magnesium alloys, *Metall. & Mater. Trans.* 45A (2014) 4698 – 4709.
- [11] X-M. Cheng, J.G. Morris, The anisotropy of the Portevin-Le Chaterlier effect in Aluminum alloys, *Scr. Mater.* 43 (2000) 651–658.
- [12] J. Mizera, K.J. Kurzydowski, On the anisotropy of the Portevin–Le Chaterlier plastic instabilities in Al-Li-Cu-Zr alloy, *Scr. Mater.* 45 (2001) 801–806.
- [13] R. Shabadi, S. Kumar, H.J. Roven, E.S. Dwarakadasa, Effect of specimen condition, orientation and alloy composition on PLC band parameters, *Mater. Sci. & Eng.* A382 (2004) 203–208.
- [14] Z. Kovács, N.Q. Chinh, J. Lendvai, Orientation dependence of Portevin–Le Chaterlier plastic instabilities in depth-sensing microindentation, *J. Mater. Res.* 16 (2001) 1171–1177.
- [15] C. Corby, C.H. Cáceres, P. Lukác, Serrated flow in magnesium alloy AZ91, *Mater. Sci. & Eng.* A387–389 (2004) 22–24.
- [16] G. Tingting, F. Siska, J. Cheng, M. Barnett, *J. Alloys & Compds* 731 (2018) 620–630.
- [17] J.R. Rice, Inelastic constitutive relations for solids: an internal variable theory and its application to metal plasticity. *J. Mech. Phys. Solids* 19 (1971) 433-455.

- [18] D. Peirce, R.J. Asaro, A. Needleman, Material rate dependence and localized deformation in crystalline solids, *Acta Metall.* 31 (1983) 1951 – 1976.
- [19] R.J. Asaro, Crystal plasticity, *J. Appl. Mech.-Trans. ASME*, 50 (1983) 921-934.
- [20] S. Graff, W. Brocks, D. Steglich, Yielding of magnesium: from single crystal to polycrystalline aggregates, *Intl. J. Plast.* 23 (2007) 1958–1978.
- [21] Y. Huang, A user-material subroutine incorporating single crystal plasticity in the ABAQUS finite element program, Cambridge, Massachusetts, 1991.
- [22] M. Werwer, A. Cornec, Numerical simulation of plastic deformation and fracture in polysynthetically twinned (PST) crystals of TiAl. *Comput. Mater. Sci.* 19 (2000) 97-107.
- [23] C.H. Càceres, D.M. Rovera, Solid solution strengthening in concentrated Mg–Al, *J. Light Metals*, 1 (2001) 151–156.
- [24] N. Stanford, M.R. Barnett, Solute strengthening of prismatic slip, basal slip, and  $\{10\bar{1}2\}$  twinning in Mg and Mg–Zn binary alloys, *Intl. J. Plast.* 47 (2013) 165–181.
- [25] J.A. Yasi, L.G. Hector Jr., D.R. Trinkle, First principles data for solid-solution strengthening of magnesium: from geometry and chemistry to properties, *Acta Mater.* 58 (2010) 5704–5713.
- [26] A. Akhtar, E. Teghtsoonian, Solid solution strengthening of magnesium single crystals–I: alloying behaviour in basal slip, *Acta Metall.* 17 (1969) 1339–1349.
- [27] H. Ovari, E.T. Lilleodden, Temperature dependence of plastic instability in Al alloys: A nanoindentation study, *Mater. & Design* 125 (2017) 69–75.
- [28] F.B. Klose, A. Ziegenbein, F. Hagemann, H. Neuhäuser, P. Hähner, M. Abbadi, A. Zeghloul, Analysis of Portvein-Le Chatelier serrations of type B in Al–Mg, *Mater. Sci. & Eng. A* 369 (2004) 76–81.
- [29] E. Pink, A. Grinberg, Stress drops in serrated flow curves of Al5Mg, *Acta Metall.* 30 (1982) 2153–2160.
- [30] G. Horváth, N.Q. Chinh, J. Gubicza, J. Lendvai, Plastic instabilities and dislocation densities during plastic deformation in Al–Mg alloys, *Mater. Sci. & Eng. A* 445 (2007) 186–192.
- [31] W. Zhang, Y. Gao, Y. Xia, H. Bei, Indentation Schmid factor and incipient plasticity by nanoindentation pop-in tests in hexagonal close-packed single crystals, *Acta Mater.* 134 (2017) 53–65.
- [32] M.S. Bharathi, M. Lebyodkin, G. Ananthakrishna, C. Fressengeas, L.P. Kubin, The hidden order behind jerky flow, *Acta Mater.* 50 (2002) 2813–2824.
- [33] C.A. Schuh, A.C. Lund, Application of nucleation theory to the rate dependence of incipient plasticity during nanoindentation, *J. Mater. Res.* 19 (2004) 2152–2158.

- [34] J.R. Morris, H. Bei, G.M. Pharr, E.P. George, Size effects and stochastic behaviour of nanoindentation pop in, *Phys. Rev. Lett.* 106 (2011) 165502.
- [35] L.Y. Chen, M. He, J. Shin, G. Richter, D.S. Gianola, Measuring surface dislocation nucleation in defect-scarce nanostructures, *Nat. Mater.* 14 (2015) 707–714.
- [36] D. Catoor, Y.F. Gao, J. Geng, M.J.N.V. Prasad, E.G. Herbert, K.S. Kumar, G.M. Pharr, E.P. George, Incipient plasticity and deformation mechanisms in single-crystal Mg during spherical nanoindentation, *Acta Mater.* 61 (2013) 2953–2965.
- [37] C.A. Schuh, T.G. Nieh, A nanoindentation study of serrated flow in bulk metallic glasses, *Acta Mater.* 51 (2003) 87–99.
- [38] H. Kitahara, T. Mayama, K. Okumura, Y. Tadano, M. Tsushida, S. Ando, Anisotropic deformation induced by spherical indentation of pure Mg single crystals, *Acta Mater.* 78 (2014) 290–300.
- [39] P. Gugliemi, M. Ziehmer, E.T. Lilleodden, On a novel strain indicator based on uncorrelated misorientation angles for correlating dislocation density to local strength, *Acta Mater.* 150 (2018) 195–205.
- [40] B. Selvarajou, J. Shin, T. K. Ha, I. Choi, S. P. Joshi, H. N. Han, Orientation-dependent indentation response of magnesium single crystals: Modeling and experiments, *Acta Mater.* 81 (2014) 358–376.
- [41] J.K. Mason, A.C. Lund, C.A. Schuh, Determining the activation energy and volume for the onset of plasticity during nanoindentation, *Phys. Rev.* B73 (2006) 054102.
- [42] L.Y. Chen, M. He, J. Shin, G. Richter, D.S. Gianola, Measuring surface dislocation nucleation in defect-scarce nanostructures, *Nature Mater.* 14 (2015) 707–714.
- [43] E.T. Lilleodden, Microcompression study of Mg (0 0 0 1) single crystal, *Scri. Mater.* 62 (2010) 532–535.
- [44] N. Stanford, I. Sabirov, G. Sha, A. La Fontaine, S. Ringer, M. Barnett, Effect of Al and Gd solutes on the strain rate sensibility of magnesium alloys, *Metall. Mater. Trans. A* 41 (2010) 734–743.
- [45] G. Garces, A. Munoz-Morris, D.G. Morris, P. Perez, P. Adeva, An examination of strain aging in a Mg–Y–Zn alloy containing Gd, *J. Mater. Sci.* 50 (2015) 5769–5776.

- [46] L. Jiang, J.J. Jonas, R. Mishra, Effect of dynamic strain aging on the appearance of the rare earth texture component in magnesium alloys, *Mater. Sci. Eng. A* 528 (2011) 6596–6605.
- [47] T.Q. Li, Y.B. Liu, Z.Y. Cao, R.Z. Wu, M.L. Zhang, L.R. Cheng, D.M. Jiang, The twin mechanism of Portevin Le Chatelier in Mg–5Li–3Al–1.5Zn–2RE alloy, *J. Alloys and Cmpds* 509 (2011) 7607–7610.
- [48] M. Fronzi, H. Kimizuka, S. Ogata, Atomistic investigation of vacancy assisted diffusion mechanism in Mg ternary (Mg – RE – M) alloys, *Comp. Mater. Sci.* 98 (2015) 76–82.
- [49] M.A. Soare, W.A Curtin, Single-mechanism rate theory for dynamic strain aging in FCC metals, *Acta Mater.* 56 (2008) 4091–4101.
- [50] P. Yi, R.C. Cammarata, M.L. Falk, Solute softening and defect generation during prismatic slip in magnesium alloys, *Modelling Simul. Mater. Sci. Eng.* 25 (2017) 085001.
- [51] Z. Wu, W.A. Curtin, The origins of high hardening and low ductility in magnesium, *Nature* 526 (2015) 62–67.
- [52] S. Ganeshan, L.G. Hector Jr., Z.-K. Liu, First-principles calculations of impurity diffusion coefficients in dilute Mg alloys using the 8-frequency model, *Acta Mater.* 59 (2011) 3214–3228.
- [53] M.F. Ashby, The deformation of plastically non-homogeneous materials, *Phil. Mag.* 21 (1970) 399–424.

## Supplementary Material

Table S1: Self-hardening parameters used for the CPFEM simulation. The values were taken from Ref. [20].

	<b>Basal</b> $\langle a \rangle$	<b>Prismatic</b> $\langle a \rangle$	<b>Pyramidal 2</b> $\langle a + c \rangle$	<b>Tensile twinning</b>
<b>Hardening law</b>	Linear	Voce	Voce	linear + power
$\tau_0$ [MPa]	1	20	40	5
$\tau_\infty$ [MPa]	-	150	260	-
$h_0$ [MPa]	10	7500	7500	200
$\gamma_{\text{ref}}$ [-]	-	-	-	0.11
$m$ [-]	-	-	-	10

Table S2: Interaction (latent) hardening parameters,  $q_{\alpha\beta}$ , used for the CPFEM simulation. The values were also taken from Ref. [20].

$\beta \backslash \alpha$	<b>Basal</b> $\langle a \rangle$	<b>Prismatic</b> $\langle a \rangle$	<b>Pyramidal 2</b> $\langle a + c \rangle$	<b>Tensile twinning</b>
<b>Basal</b> $\langle a \rangle$	0.2	0.5	0.5	0.5
<b>Prismatic</b> $\langle a \rangle$	0.2	0.2	0.2	0.5
<b>Pyramidal 2</b> $\langle a + c \rangle$	1.0	1.0	0.2	0.25
<b>Tensile twinning</b>	1.0	1.0	0.2	0.25

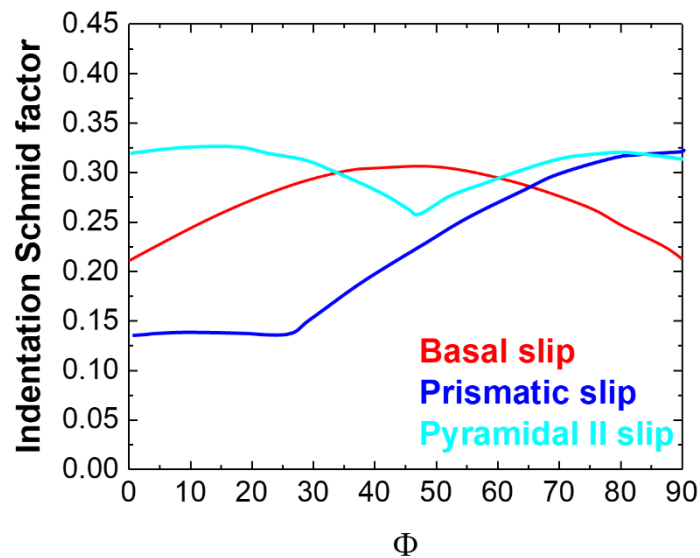


Fig. S1: Indentation Schmid factors (ISF) for activation of slip in the basal, prismatic and pyramidal II planes of Mg as a function of the angle between the normal to a given plane and the c-axis,  $\Phi$ . The curves were taken from Ref. [31]. For simplicity, only portions of the curves with the highest ISF among all possible slip systems are shown.

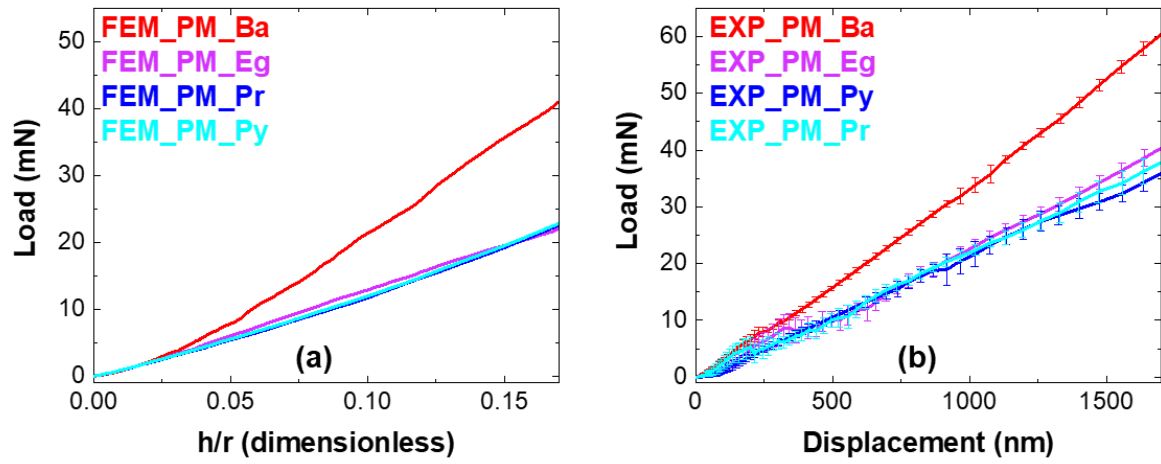


Fig. S2: Load (P) vs. Displacement (h) response of Pure Mg:  
 (a) obtained from crystal plasticity based finite element method (CPFEM). The simulations were made on the crystal planes with same orientations as the AZ91 sample.  
 (b) obtained from spherical nanoindentation experiments on similar orientations. Both experiment and simulation show very similar trend.